Enabling Lasing Action in Hybrid Atomic–Nanophotonic Integrated Structures

Hadiseh Alaeian,* Brian C. Odom, and Jorge Bravo-Abad*

The incorporation of neutral atoms in nanophotonic structures offers significant potential to realize novel quantum optical devices. Here, the possibility of creating low-threshold integrated lasers in hybrid systems is investigated based on coupling room-temperature atomic gases with both dielectric and metallic nanophotonic systems. The particular focus on studying two different classes of devices resulting from incorporating an optically pumped Rb–ethane mixture in a dielectric ring resonator and a plasmonic lattice. It is shown that the combination of the optical gain provided by the atomic vapor, along with the unique field-confinement properties of nanophotonic structures, enables the generation of coherent radiation, that is, laser light, at moderate power levels. In addition, general design guidelines for these hybrid nanophotonic lasers are provided. These results pave the way toward a novel class of active nanophotonic and metamaterial systems.

1. Introduction

The field of quantum optics has greatly benefited from theoretical and technological advances in nanophotonics. With the first demonstration of single photon sources in a nanodevice at the beginning of this century,[1–5] these systems became one of the prominent platforms for realizing various quantum optical phenomena and devices. Low-threshold photonic crystal lasers,[6–8] plasmonic nanolasers,[9–13] strong coupling,[14–16] photon blockade,[17–19] chiral quantum optics, and entanglement[20–23] are some of the intriguing quantum optical phenomena studied and realized in solid-state photonic platforms. In spite of their appealing features for integration as a monolithic module, the large crystal-field broadening and the heterogeneity of quantum dots have been two major bottlenecks of solid-state systems in achieving long coherence length and large-scale quantum networks.[24]

Dr. H. Alaeian, Prof. B. C. Odom
Department of Physics and Astronomy
Northwestern University
Evanston, IL, 60208, USA
E-mail: alaeian@alumni.stanford.edu

Prof. J. Bravo-Abad
Departamento de Física Teórica de la Materia Condensada and Condensed Matter Physics Center (IFIMAC)
Universidad Autónoma de Madrid
E-28049, Madrid, Spain
E-mail: jorge.bravo@uam.es

ⓘD The ORCID identification number(s) for the author(s) of this article can be found under https://doi.org/10.1002/andp.201800203

Meanwhile, in parallel, substantial developments in other disciplines of physics have been made toward realizing different quantum information processing schemes. In particular, in the realm of atomic, molecular, and optical physics (AMO), trapped ions and neutral atoms have been employed as high-fidelity nodes and qubits in scalable quantum computers.[25–29] To date, AMO systems are one of the most ideal known candidates regarding their coherence features, with very well-established and precise quantum state manipulation schemes. On the other hand, thanks to the advances in nanotechnology and fabrication techniques, nanophotonic structures provide optimal platforms for integration and scalability. Therefore, a new promising approach could benefit from the best of two worlds, in a hybrid scheme on the interface between AMO and nanophotonics.[30]

Among different candidates in AMO, neutral atoms are easier to work with, since the presence of a device in the vicinity of ions would substantially perturb the ion traps due to the induced surface charges. Moreover, in spite of some successful demonstrations of cold atom–photonic device couplings, the miniaturization of the typical cold atom setups compatible with nanodevices is still a challenge.[31–33] Unlike cold atoms, thermal vapors lend themselves for proper integration and coupling to photonic modes, as has been demonstrated in hollow-core fibers and waveguides.[34–36] Very recently, thermal vapors of alkali atoms have been successfully combined with on-chip, integrated plasmonic and photonic devices where the atomic transitions have been modified with photonic modes, showing noticeable effects, such as Fano resonances and sub-Doppler line modifications.[37–39]

In this work, we investigate the possibility of laser light generation in hybrid systems that combine room-temperature atomic clouds and nanophotonic structures. The optical gain we consider in our study consists of an optically pumped mixture of Rb and ethane, as has been successfully employed in the past in diode pumped alkali lasers (DPAL) for achieving large optical gain within the infrared.[40–42] This Rb–ethane mixture is incorporated into two different classes of integrated nanophotonic platforms, an all-dielectric ring resonator supporting whispering gallery modes (WGMs) with a large quality factor,[43] and a plasmonic lattice, featuring lattice resonances with moderate quality factor and large field enhancement at the subwavelength scale.[44]
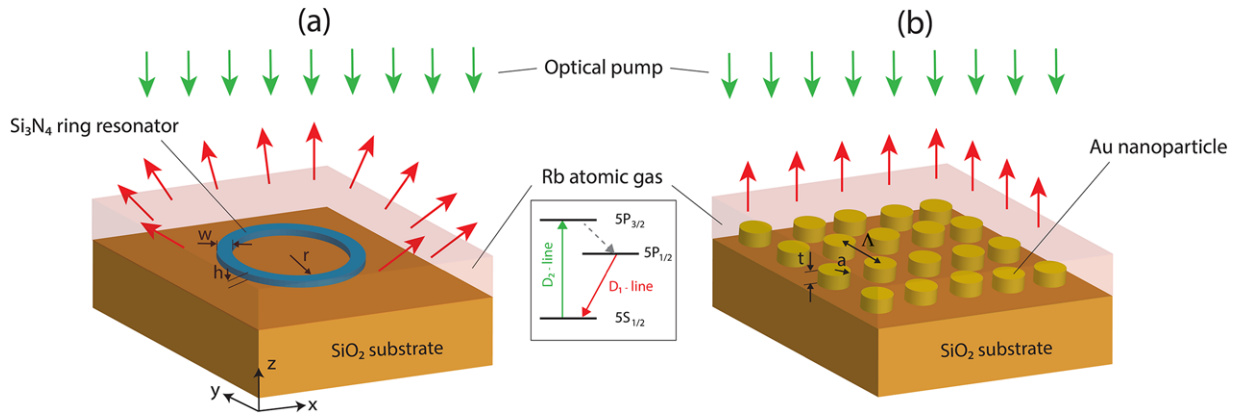
Figure 1. a,b) Schematics of the ring resonator (a) and plasmonic hybrid laser (b) systems studied in this work. The geometrical parameters defining each structure are also included in the figure. Top green arrows in (a) and (b) represent the external pumping, while the red arrows represent the laser emission. The central inset shows the energy-level diagram of the Rb atoms forming the gain medium.

To tackle this problem, we apply an efficient density matrix-based formalism that properly captures the dynamics and decoherence of light–matter interaction in the studied systems. Using this approach, we show how the temporal and spatial field-confinement properties of the considered nanophotonic systems can be tailored to enable laser light emission at low pumping power levels. Furthermore, we derive a simplified model that provides general design guidelines for this novel class of hybrid active systems.

2. Theoretical Framework

In spite of their very different wavelengths, all DPALs share the same working principle. The outer shell of alkalis have three main electronic levels of $n\,^2S_{1/2}$, $n\,^2P_{1/2}$, $n\,^2P_{3/2}$. In a mixture with alkali atoms excited at D_2-line (i.e., $n\,^2P_{3/2}$), the collision of the excited atoms with the molecules of a buffer gas (typically a hydrocarbon) efficiently transfers part of the population from the excited state to $n\,^2P_{1/2}$. With a properly chosen buffer gas at an optimized pressure, population inversion between levels $n\,^2P_{1/2}$ and $n\,^2S_{1/2}$ builds up and, hence, optical gain at this transition (known as D_1-line) is established.[42]

To model the interaction of this atomic cloud with photonic modes we apply a semi-classical approach, where the electromagnetic fields are treated classically and the atoms are considered quantum mechanically.[45] In particular, for the considered class of systems, the density matrix is the most suitable approach to account for all of the atomic transitions and decoherence phenomena, such as Doppler and transient broadening.[46] Moreover, if the additional decoherence mechanisms such as collision of Rb atoms with buffer gas molecules are considered in Lindblad form, the Liouville equation properly describes the time evolution of the atomic states when coupled to an arbitrary photon field. In what follows we describe the theoretical method used to simulate our hybrid lasing systems, where the gain medium (formed by a mixture of Rb vapor and buffer gas) is treated as a three-level system as shown in **Figure 1** (Rb electronic levels $5S_{1/2}$, $5P_{1/2}$, and $5P_{3/2}$ will be denoted by $|1\rangle$, $|2\rangle$ and $|3\rangle$, respectively). Note that, due to collisional broadening with the buffer gas molecules, the considered atomic vapor can be properly de-

scribed as a three-level gain medium.[41,42] Moreover, although the final equations and results have been derived for a three-level gain medium and single mode cavities, the procedure can be generalized for more atomic levels and multi-mode photonic systems.[47–50]

The time evolution of the Rb atom density matrix ($\hat{\rho}$) is described via the following Liouville equation.

$$\dot{\hat{\rho}} = -\frac{i}{\hbar}[\hat{H}_A + \hat{H}_I, \hat{\rho}] + \mathcal{L}[\hat{\rho}] \tag{1}$$

where $\hat{H}_A$ is the free-atom Hamiltonian and $\hat{H}_I$ is the interaction Hamiltonian describing the coupling between the atoms and the cavity field.

The cavity field $\vec{E}(\vec{r}, t)$ is determined via Maxwell's equation as

$$\left(\nabla^2 - \frac{\epsilon_r(\vec{r})}{c^2}\frac{\partial^2}{\partial t^2}\right)\vec{E}(\vec{r}, t) = \mu_0 \frac{\partial^2 \vec{P}(\vec{r}, t)}{\partial t^2} \tag{2}$$

In the above equation, $\epsilon_r(\vec{r})$ is the linear permittivity, which in a nanophotonic structure is, in general, a function of position. $\vec{P}(\vec{r}, t)$ is the polarizability of the atomic cloud. For a uniform atomic density of N, $\vec{P}(\vec{r}, t)$ is related to the induced atom dipole moment, $\vec{p}(\vec{r}, t)$, by

$$\vec{P}(\vec{r}, t) = N\langle\vec{p}(\vec{r}, t)\rangle = \text{Tr}(\hat{p}\hat{\rho}(\vec{r}, t))N = N(\rho_{21}(\vec{r}, t)\vec{M} + c.c.) \tag{3}$$

where $\vec{M}$ is the transition electric dipole moment between states $|1\rangle$ and $|2\rangle$ (we implicitly assume that the coherent atom-field interaction only occurs between those states). The interaction between levels $|1\rangle$ and $|3\rangle$ is assumed to be incoherent and can be described through an effective pumping rate R_p.

On the other hand, $\vec{E}(\vec{r}, t)$ can be expanded in terms of cold-cavity modes at ω_c with decay rate γ_c

$$\vec{E}(\vec{r}, t) = \vec{E}^+(\vec{r}, t) + c.c. = \vec{E}_0^+(\vec{r})e^{-\gamma_c t}e^{-i\omega_c t} + c.c. \tag{4}$$

After properly incorporating the finite lifetime of each state, and within the validity realm of the rotating wave approximation

(RWA), one can obtain the following sets of equations of motion for the density matrix elements

$$\dot{\rho}_{33}(\vec{r}, t) = -(\gamma_{31} + \gamma_{32})\rho_{33}(\vec{r}, t) + R_p(\rho_{11}(\vec{r}, t) - \rho_{33}(\vec{r}, t)) \quad (5a)$$

$$\dot{\rho}_{22}(\vec{r}, t) = \gamma_{32}\rho_{33}(\vec{r}, t) - \gamma_{21}\rho_{22}(\vec{r}, t) + \frac{1}{i\hbar}(\vec{M} \cdot \vec{E}^-(\vec{r}, t)e^{i\omega_c t}\rho_{21}(\vec{r}, t) - c.c.) \quad (5b)$$

$$\dot{\rho}_{11}(\vec{r}, t) = \gamma_{31}\rho_{33}(\vec{r}, t) + \gamma_{21}\rho_{22}(\vec{r}, t) - R_p(\rho_{11}(\vec{r}, t) - \rho_{33}(\vec{r}, t)) - \frac{1}{i\hbar}(\vec{M} \cdot \vec{E}^-(\vec{r}, t)e^{i\omega_c t}\rho_{21}(\vec{r}, t) - c.c.) \quad (5c)$$

$$\dot{\rho}_{21}(\vec{r}, t) = -(i\omega_a + \gamma_\perp)\rho_{21}(\vec{r}, t) + \frac{1}{i\hbar}\vec{M}^* \cdot \vec{E}^+(\vec{r}, t)e^{-i\omega_c t}w(\vec{r}, t) \quad (5d)$$

where $\gamma_\perp = \gamma_{32} + \frac{\gamma_{21}}{2}$ is the transverse decoherence rate taking into account all the decoherence effects, including the collision with the buffer gas. ω_a is the atomic frequency, and $w(\vec{r}, t) = \rho_{22}(\vec{r}, t) - \rho_{11}(\vec{r}, t)$ is the population difference between energy levels $|2\rangle$ and $|1\rangle$.

In contrast to macroscopic photonic cavities, where the uniform field approximation can be used, in nanophotonic and plasmonic structures one cannot ignore the spatial variation of the electromagnetic fields inside the system, as the field features vary below or on the order of the wavelength. That makes the density matrix elements functions of both time and position. In other words, the above sets of equations have to be solved simultaneously at each point of the space to properly capture all the atomic and photonic features. To overcome this, we project the fields of the hybrid system on the basis of the cold-cavity modes.[49] Therefore, the modified cavity field can be rewritten as

$$\vec{E}(\vec{r}, t) = E_0 (\vec{f}_0^+(\vec{r}) a^+(t) e^{-i\omega_c t} + c.c.) \quad (6)$$

where we have defined $E_0 = \max[\vec{E}_0^+(\vec{r})|]$ and the dimensionless vectors $\vec{f}_0^\pm(\vec{r}) = \vec{E}_0^\pm(\vec{r})/E_0$.

For the observables appearing as diagonal elements of the density matrix, the spatially averaged parameters can be calculated as

$$\langle \rho_{ii}(t) \rangle = \frac{\int_{atom} dv\, \rho_{ii}(\vec{r}, t)\, |\vec{f}_0^+(\vec{r})|^2}{\int_{atom} dv\, |\vec{f}_0^+(\vec{r})|^2} \quad (7)$$

The subscript "atom" in the above integral indicates an integration over the active region where the polarizable atoms are present. For the off-diagonal elements related to coherence, we apply the following assumption within the active region

$$\vec{M}\rho_{21}(\vec{r}, t) = |\vec{M}|\, \vec{f}_0^+(\vec{r})\, e^{-i\omega_a t}\, \tilde{\rho}_{21}(t) \quad (8)$$

The above definitions, combined with Equations (5a–5d) and (2), allow us to rewrite the equations of motion for the problem as

$$\frac{d\langle\rho_{33}\rangle}{dt} = -(\gamma_{31} + \gamma_{32})\langle\rho_{33}\rangle + R_p(\langle\rho_{11}\rangle - \langle\rho_{33}\rangle) \quad (9a)$$

$$\frac{d\langle\rho_{22}\rangle}{dt} = \gamma_{32}\langle\rho_{33}\rangle - \gamma_{21}\langle\rho_{22}\rangle + \frac{\zeta}{i\hbar}(\tilde{\rho}_{21}a^-(t)e^{i\delta t} - c.c.) \quad (9b)$$

$$\frac{d\tilde{\rho}_{21}}{dt} = -\gamma_\perp\tilde{\rho}_{21} + \frac{1}{i3\hbar}|\vec{M}|E_0\langle w\rangle a^+(t)e^{-i\delta t} \quad (9c)$$

$$\frac{d}{dt}a^+(t) = -\gamma_c a^+(t) + \left[i\frac{\omega_a}{2}\tilde{\rho}_{21} - \frac{d}{dt}\tilde{\rho}_{21}\right]\mu_0 Nc^2\xi\frac{\omega_a}{\omega_c}e^{i\delta t} \quad (9d)$$

where $\delta = \omega_c - \omega_a$ is the detuning between the cavity resonance and the atomic frequency. The parameters ζ and ξ describe the effective interaction of the field with the active region of the system and are defined as $\xi = (|\vec{M}|/E_0)\zeta_1$ and $\zeta = |\vec{M}|E_0\zeta_2$, with

$$\zeta_1 = \frac{\int_{atom} dv\, |\vec{f}_0^+(\vec{r})|^2}{\int_{space} dv\, \epsilon(\vec{r})\, |\vec{f}_0^+(\vec{r})|^2} \quad (10a)$$

$$\zeta_2 = \frac{\int_{atom} dv\, |\vec{f}_0^+(\vec{r})|^4}{\int_{atom} dv\, |\vec{f}_0^+(\vec{r})|^2} \quad (10b)$$

The above equations are general and can be used to describe the interaction of the atom cloud with arbitrary fields of a nanodevice in any configuration. To solve for the lasing features, Equation (9a–d) must be solved with the following initial conditions when a proper pumping exists[51]

$$\rho_{11}(0) = 1,\ \rho_{22}(0) = \rho_{33}(0) = a^+(0) = 0,\ R_p \neq 0 \quad (11)$$

All of the unknown variables in Equation (9a–d) are time-dependent only, making the atom–cavity interaction problem more tractable numerically, while providing more physical insight. Finally, note that a standard rate equation analysis can be derived from Equation (9a–d) by adiabatically eliminating the coherence term from Equation (9c).

3. Results and Discussion

3.1. Description of the Analyzed Systems and Their Passive Responses

Figure 1 shows schematic views of the two hybrid laser systems under study. The first configuration (Figure 1a) consists of a dielectric Si_3N_4 ring of inner radius r, height h, and width w, lying on top of a SiO_2 substrate. The dielectric ring is embedded in a thermal cloud formed by a mixture of Rb atoms (of density N) and ethane molecules. The Rb atoms are modeled as three-level systems, excited with an incoherent pump at $\lambda_{D_2} = 780$ nm. The fast and non-radiative transition between $5P_{3/2}$ and $5P_{1/2}$ states (mainly achieved via collision with the ethane buffer gas molecules) enables population inversion between this level and the ground state to be built up at the D_1-transition, with $\lambda_{D_1} = 795$ nm (see the corresponding energy-level diagram in inset of Figure 1). The second considered structure is a periodic lattice of gold cylindrical nanoparticles (Figure 1b). The lattice constant is given by Λ, and the radius and height of each of the nanoparticles are a and t, respectively. The rest of the details are the same as those described for the ring-resonator case.
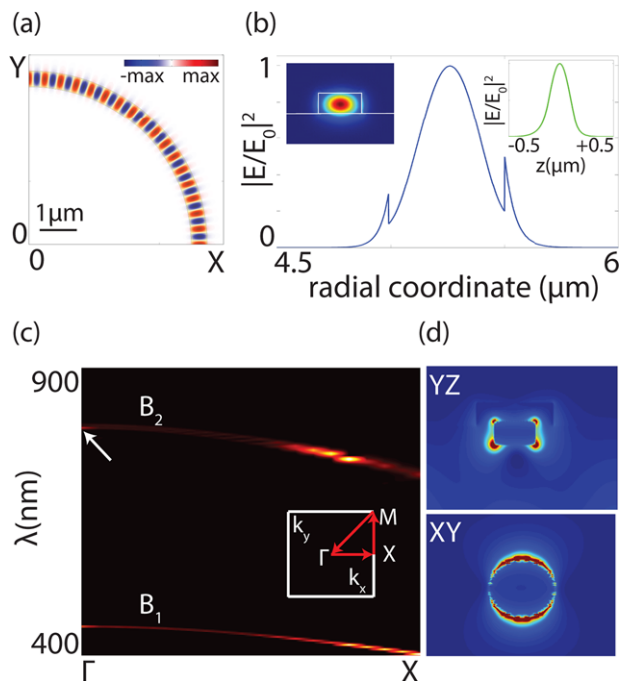
**ADVANCED
SCIENCE NEWS**

www.advancedsciencenews.com

*annalen
der* **physik**

www.ann-phys.org

Figure 2. a) Magnetic field amplitude (H_z) at $\lambda = 795$ nm (Rb D_1-line) in the xy-plane at the center of the dielectric microring shown in Figure 1a. For illustration, only one quadrant of the microring is displayed. The geometrical parameters of the structure are $r = 5$ μm, $w = 500$ nm and $h = 250$ nm. b) Radial variation of the normalized E-field intensity of the mode shown in (a). Left inset displays a yz cross-section of the E-field intensity, while the right inset shows the variation of the same quantity along the z-axis. c) Band diagram of the plasmonic lattice shown in Figure 1b, calculated along the ΓX direction in the first Brillouin zone (see inset) assuming $\Lambda = 450$ nm, $t = 60$ nm, and $a = 45$ nm. Two plasmonic bands (labeled as B_1 and B_2), located within the visible and infrared range, are shown. d) yz (top) and xy (bottom) cross-sections of the E-field intensity of the plasmonic mode near $\lambda = 795$ nm (indicated by the white arrow in (c)).

To get physical insight into the lasing features of the studied systems, we focus first on analyzing the cold-cavity features in the absence of Rb atoms. **Figure 2**a,b summarize the results for the ring resonator. In these calculations we have assumed refractive indexes of $n = 2.00$ and $n = 1.45$ for the Si_3N_4 and SiO_2 regions of the structure, respectively, and the following geometrical parameters: $r = 5$ μm, $w = 500$ nm, and $h = 250$ nm. These values have been obtained by optimizing simultaneously the ring radius and the azimuthal order m of the WGMs, until tuning a high-order WGM to the D_1-line of Rb (i.e., until $\delta = 0$ is obtained). The effect of a non-zero detuning of the WGM resonance with respect to the atomic transition will be discussed later in the text. Further details on the optimization process are included in the Supporting Information, where the influence of r and m on the modal resonance is described.

Figure 2a shows a cross-section along a xy-plane (at the center of the microring) of the magnetic field amplitude (H_z) of the TE-polarized WGM with $m = 68$ supported by the optimal structure at $\lambda = 795$ nm. The corresponding electric field intensity distribution is shown in Figure 2b. As can be seen, most of the E-field is concentrated inside the dielectric ring, but still there

are fractions of the field extending beyond the ring and interacting with the atomic cloud. Similarly, Figure 2c,d depicts the results for the plasmonic lattice shown in Figure 1b, calculated for $\Lambda = 450$ nm, $t = 60$ nm, and $a = 45$ nm. The substrate is assumed to be SiO_2 and the metallic gold nanoparticles are described with available empirical data.[52] Figure 2c displays the band diagram of the periodic lattice along the $\Gamma - X$ direction of the first Brillouin Zone (see the inset of Figure 2c). This band diagram was obtained through a Fourier transform analysis of the slowly decaying eigenmodes of the system after being excited by a set of point dipoles located at random positions (we carried out this analysis using the finite-difference-time-domain implementation provided by Lumerical, see Supporting Information for details).

Two plasmonic bands exist in the spectrum. The mode of our interest is the one at $\lambda = 795.18$ nm for $k_x = 0$ (indicated with a white arrow in main panel of Figure 2c). As in the case of the ring resonator, the geometrical parameters of the plasmonic lattice have been optimized so that the *lattice plasmon resonance* (formed by the hybridization of the diffracted lattice modes with the localized surface plasmon resonances of each metallic nanoparticle) appears as close as possible to the D_1-transition of Rb. Due to their larger Q-factor in comparison with other plasmonic resonances, lattice plasmons have been successfully used in the past for realizing plasmon-assisted lasers.[53–56] Figure 2d shows the cross-sections of the E-field distribution of the plasmonic lattice mode, which illustrates the large field enhancements associated to this class of resonances. Finally, we highlight that, in contrast to the ring resonator, and due to the intrinsic characteristics of the lattice plasmons, it is not possible to fully tune these modes to the desirable atomic resonance while keeping the geometrical parameters in a realistic range. The implications of this on the laser performance and dynamics are discussed in Section 3.3. Finally, we point out that the highly non-uniform field distributions characterizing the considered structures lead to fundamental differences of their effective response with respect to what is expected in bulk configurations.[49]

3.2. Laser Dynamics and Steady-State Characteristics

In this section, we consider the behavior of the resonators designed in the previous section in the vicinity of the atomic vapor and buffer gas mixture. The buffer gas leads to a rapid dephasing of both Rb isotopes, producing a homogeneous broadening on the order of several tens of gigahertz, which strongly depends on the buffer gas pressure. Here we considered a 12 GHz line width due to this phenomenon. We further assume that these buffer gas-induced dephasing rates are the same for all transitions.[57] In the following calculations, we assume a transition dipole moment of Rb of $|\vec{M}| = 25 \times 10^{-30}$ C m[58] and a gas density of $N = 10^{22}$ m^{-3}. This value for the density is chosen just for illustration purposes. As we show below, the considered structures can display lasing action at lower vapor densities. Further reduction in the density of the gain medium could be achieved by designing nanophotonic devices where the atoms are interacting with high-intensity electric fields, rather than with the evanescent tail of the field (for instance, an inverted ring-resonator structure
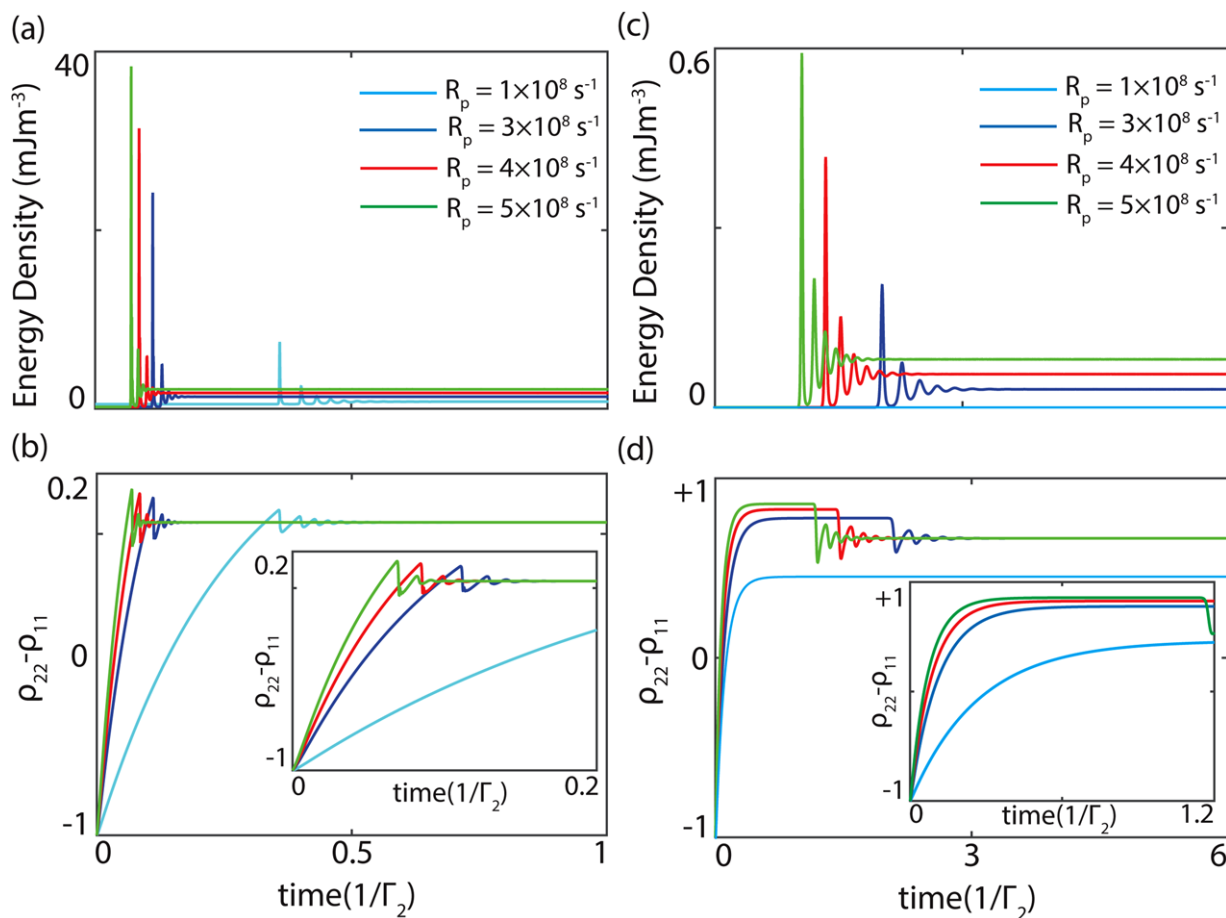
Figure 3. a) Variation of the electric field energy density and b) population difference between energy levels $|2\rangle$ and $|1\rangle$ as a function of time, computed for the ring-resonator structure shown in Figure 1a at various pumping rates. c,d) Same as (a) and (b), respectively, but for the plasmonic lattice shown in Figure 1b. Insets in (b) and (d) show the dynamical behavior of the population difference at early times, illustrating the fast increase of the excited state population. The normalizing factor $\Gamma_2 = 36 \times 10^6 \ s^{-1}$ is the natural decay rate of level $|2\rangle$.

optimized to make the atoms interact with the intense electric field within the slot could be a potential promising candidate.).

Figure 3 summarizes the dynamical characteristics of the coupled atom-cavity system. Figure 3a,c show the time evolution of the spatially averaged electric energy density of the studied ring resonator and plasmonic lattice, respectively. Results for four different pumping rates, ranging from $R_p = 1.0 \times 10^8 \ s^{-1}$ (light blue line) to $R_p = 5.0 \times 10^8 \ s^{-1}$ (green line), are shown. In both systems, we obtain the canonical features of lasing dynamics, consisting of a series of sudden spikes in the field energy signal that settle down to a non-zero value in steady state, indicating that both systems can indeed lase at large enough pumping rates. In addition, as seen in Figure 3a,c, our results show that the microring cavity displays shorter lasing onset times and faster oscillations than the plasmonic lattice. At $R_p = 5 \times 10^8 \ s^{-1}$, the ring resonator takes 3.3 ns to reach to the steady state, while this time increases to 65 ns (about 20 times longer) for the plasmonic lattice.

To investigate the link between the field oscillations and population of the electronic levels in Rb atoms, Figure 3b,d show the corresponding time evolution of the spatially averaged population inversion ($\rho_{22} - \rho_{11}$). In both cases, before the first lasing spike occurs, the averaged population inversion rapidly grows

with time (see insets of Figure 3b,d). This corresponds to the regime where the population of $|2\rangle$ is increasing (the system is *accumulating* population inversion). When the population difference between $|2\rangle$ and $|1\rangle$ becomes large enough, so its associated optical gain can overcome all the decoherence phenomena, the first burst of laser radiation takes place, as can be observed in Figure 3b,d for the larger values of R_p. This burst leads to a significant depletion of the population inversion (a significant amount of the upper-level population decays via stimulated emission), leading in turn to a dramatic drop of the cavity field intensity. After that, a subsequent recovery of the population inversion begins, until enough population inversion is accumulated again and a second spike of the signal occurs. This is accompanied by a corresponding drop in the population inversion. This series of bursts and subsequent drops of the populations inversion takes place sequentially (smoother spikes and drops of the lasing signal and population inversion are obtained for larger times) until a steady state is reached. The steady-state value of the population inversion required for lasing depends on the decoherence phenomena in the gas as well as the optical cavity.

In this context, it is also useful to consider the small-signal gain regime. In particular, by assuming $a^+ = 0$ in Equation (9a–d),

**ADVANCED
SCIENCE NEWS**
www.advancedsciencenews.com

annalen
der **physik**
www.ann-phys.org

we obtain the following analytical expression for the population inversion.

$$\rho_{22} - \rho_{11} = \frac{R_p(\gamma_{32} - \gamma_{21}) - \gamma_{21}\Gamma_3}{R_p(2\gamma_{21} + \gamma_{32}) + \gamma_{21}\Gamma_3} \tag{12}$$

where $\Gamma_3 = \gamma_{32} + \gamma_{31}$ is the total decay from level $|3\rangle$. From the above equation it is clear that, in this regime, $w = \rho_{22} - \rho_{11}$ is the small-signal rate of amplification of a photon entering the atomic vapor region. Therefore, when $\gamma_c/w < 1$, the cavity mode experiences a net gain, which is responsible for the initial amplification of the cavity photon. When the number of photons in the cavity increases, the small-signal gain is not valid anymore and one needs to use the physical arguments provided above to account for the laser dynamics of the system.

After reaching the threshold, the optical gain is clamped and the population inversion remains fixed. The better the cavity, the smaller the decoherence, hence smaller gain and population inversion are required. For the ring resonator (with quality factor $Q = 3 \times 10^4$) the required fractional population inversion of lasing is approximately 0.04. While due to the lower quality factor of the lattice plasmon resonance ($Q = 211$), this value increases to 0.66. **Figure 4**a,b show the steady-state behavior of the electric-field energy density and the population difference as a function of R_p for the microring and the plasmonic lattice, respectively. The observed linear dependence above threshold confirms that the two considered configurations are indeed lasing. In addition, as seen in Figure 4, the plasmonic lattice starts to lase at the pumping threshold of $R_p^{th} = 1.9 \times 10^8 \, s^{-1}$, while the same parameter reduces to $R_p^{th} = 4.1 \times 10^7 s^{-1}$ for the microring, which is about five times smaller. These values correspond to pump powers of 48 and 10 pW power per atom in the case of the plasmonic lattice and the ring resonator, respectively.

3.3. Simplified Model

To develop further insight into the performance of the studied hybrid lasers, we use a simplified analytic model that captures the main lasing characteristics of these systems. From Equation (9a–d), we can calculate the population difference between levels $|1\rangle$ and $|2\rangle$ required to overcome all decoherence phenomena in the atom–cavity system as

$$w_{ss} = \frac{6\hbar[(\gamma_c\gamma_\perp + \delta_1\delta_2)\,Re(\zeta_1) + (\delta_1\gamma_\perp - \delta_2\gamma_c)\,Im(\zeta_1)]}{(\omega_a + 2\delta_2)\,N|\vec{M}|^2\mu_0 c^2\omega_a/\omega_c|\zeta_1|^2} \tag{13}$$

where $\delta_{1,2}$ represents the frequency pulling effect due to a non-zero frequency detuning between cavity and atom resonances, defined by $a^+(t) \to a^+(t)e^{+i\delta_1 t}$ and $\tilde{\rho}_{21}(t) \to \tilde{\rho}_{21}(t)e^{-i\delta_2 t}$. In addition, one can find that the population inversion given in Equation (13) can be achieved with an incoherent pumping of rate $R_p^{th} = \gamma_{21}(1 + w_{ss})/(1 - w_{ss})$.

Equation (13) shows that, as expected, w_{ss} depends on the longitudinal and transverse decay rates (γ_c, $\gamma_\perp$), the frequency detuning ($\delta_{1,2}$), the atom-field coherent coupling strength set by $|\mathbf{M}|$, the atom density (N), and the ratio of the active region volume to the cavity mode volume (ζ_1). In a nanophotonic cavity, ζ_1 and $\delta_{1,2}$ are strongly dependent on the device features, hence it is the

same for w_{ss}. However, we found that a good approximation to the numerical results for different types of structures can be obtained by assuming a fixed value for ζ_1. In particular, based on various studies of the two classes of considered structures, we found that $\zeta_1 = 0.04$ is a proper approximate value for both the microring and the plasmonic lattice considered in this work (see Tables S1 and S2, Supporting Information).

For a fixed atomic density of $N = 10^{22} \, m^{-3}$, **Figure 5**a,b show the behavior of w_{ss} and R_p^{th} as a function of cavity quality factor, respectively. For better understanding, the behavior has been investigated for different values of the detuning δ between the cavity resonance and the atomic transition, ranging from $\delta = 0.0$ (dark blue line) to $\delta = 0.20$ nm (light blue line). The two vertical black dashed lines mark the plasmonic lattice and ring-resonator cases (with $Q = 211$ and $Q = 3 \times 10^4$, respectively). As seen in Figure 5a, in a bad cavity regime ($Q \leq 135$), the required population inversion is ≥ 1, implying that the achievable gain in such a system is not large enough to overcome all the decoherence, hence no laser radiation can be observed within this range. The corresponding pumping rate of this region is also very high as
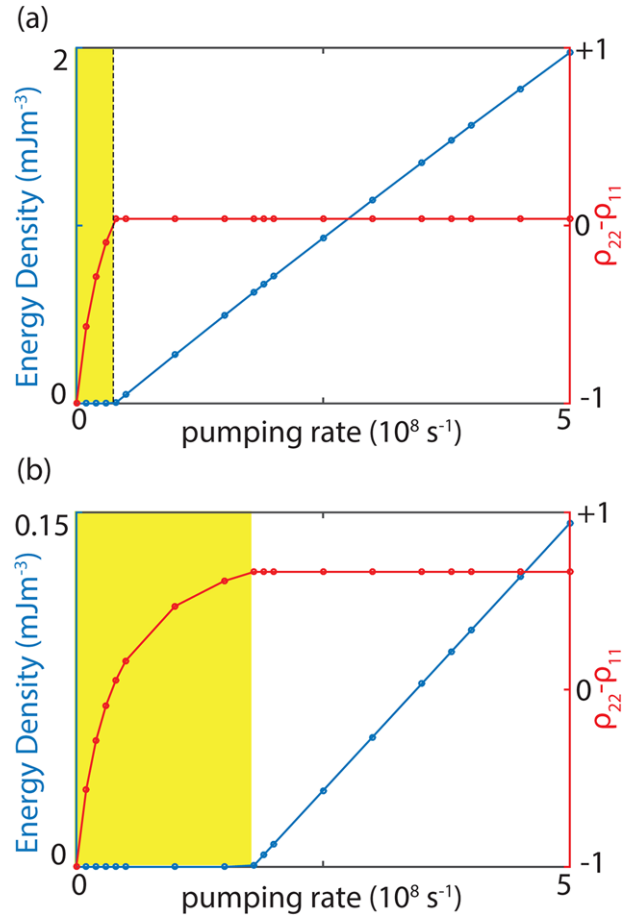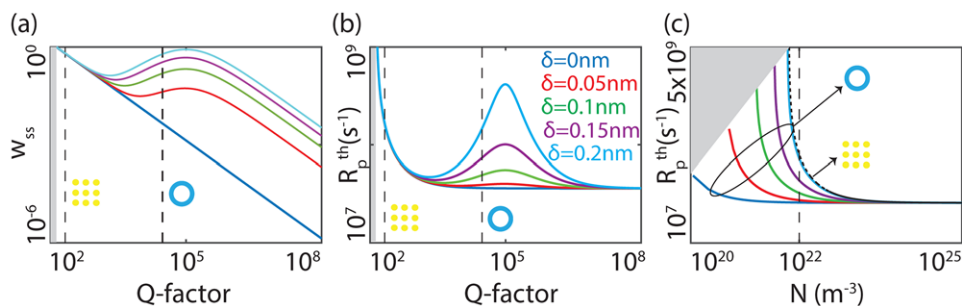

Figure 4. Calculated laser steady-state features: energy density (blue line) and the population difference (red line), as a function of the pumping rate (R_p) for the a) ring resonator and b) plasmonic lattice. The yellow region in both panels highlights the below-threshold region of the hybrid systems, where lasing does not occur.

**ADVANCED
SCIENCE NEWS**

www.advancedsciencenews.com

annalen **physik**
der

www.ann-phys.org

Figure 5. a) Required population inversion at threshold (w_{ss}) for the studied hybrid systems as a function of the quality factor (Q). The density of the atoms in the active region is $N = 10^{22}$ m^{-3} and $\zeta_1 = 0.04$ (see the definition in the main text). Results for different values of the detuning δ between the cavity resonance and the atomic transition are shown. The gray area in the low-Q part indicates the non-lasing regime, whereas the vertical black dashed lines mark the Q-factors of the plasmonic lattice and the microring studied in this work (a sketch of each structure is also included). b) Same as (a) but for the pumping rate at threshold (R_p^{th}) as a function of Q. c) Pumping rate at threshold (R_p^{th}) for the ring-resonator laser (with $Q = 3 \times 10^4$) as a function of the atomic density, N. Results for the same values of δ as in (a) and (b) are displayed. The dotted black line shows the behavior of the plasmonic lattice. The vertical dashed line marks the atomic density considered in (a) and (b).

can be seen in Figure 5b. This lasing-forbidden region is highlighted in gray in Figure 5a,b.

Structures with larger but moderate Q factors ($Q \leq 500$) lie in an intermediate region, where the inversion and pumping thresholds are almost insensitive to the atom–cavity detuning. That is due to the fact that γ_c is still too large compared to the transverse decay, so that the detuning mainly leads to a cavity pulling and not an atom pulling, making w_{ss} independent of δ. As shown in Figure 5a,b, the studied plasmonic lattice falls within this range. Hence, any further optimization of the geometrical features of the plasmonic system to decrease the detuning does not have any substantial effect in reducing the required gain or lasing threshold. For the larger quality factors, the detuning always increases the required inversion and pumping rate at threshold, as can be seen in Figure 5a,b, respectively. The microring lies within this range, where one can see the substantial sensitivity of its steady-state features as a function of detuning.

Figure 5a,b reveal an unexpected non-monotonic dependence of both population inversion and lasing threshold on Q. This behavior is a direct consequence of the frequency pulling effect. While a low Q-factor cavity tends to only detune the cavity mode resonance (i.e., $\delta_2 = 0$), a large Q-factor cavity mainly modifies the atomic resonance ($\delta_1 = 0$). For cavities with Q-factors in-between, both the atomic and cavity resonance are modified depending on the relation between γ_c and $\gamma_\perp$, leading to the non-monotonic dependence on Q shown in Figure 5a,b. To the best of our knowledge, this is the first report of such non-monotonic behavior of the lasing threshold as a function of Q in the context of active nanophotonic structures.

Figure 5c illustrates the behavior of the pumping rate at threshold as a function of the atom density. Solid lines corresponds to the studied microring structure ($Q = 3 \times 10^4$). The vertical black dashed line marks the density used throughout this paper. Different lines correspond to the different values of the detuning considered in Figure 5a,b. According to the above discussion, for a fixed atom density, the required inversion at the lasing threshold, and hence the corresponding pumping rate, should be larger for larger δ to overcome the detuning loss effect. This is precisely what is observed in Figure 5c. On the other hand, if the detun-

ing is fixed, one can increase the atom density to reduce the required stimulated emission rate from each individual atom, as corroborated by the monotonically decreasing trend displayed in Figure 5c for each value of detuning. The gray shaded area on the top-left corner indicates the parameter range where lasing cannot happen, either due to the small atom density, or due to the large detuning. Finally, the overlaid black dotted line shows the behavior of the plasmonic lattice investigated in this work ($Q = 211$). As can be seen, in spite of the very different nature of plasmonic lattice resonance modes and ring-resonator WGMs, both systems follow the same trend at large δ.

4. Conclusions

We have reported on a novel route for realizing coherent light sources in hybrid systems of alkali-buffer gas mixture and integrated nanophotonics. To study this class of systems, we have developed a theoretical method based on the density-matrix formalism, allowing us to characterize the dynamic and steady-state features of the nonlinear light–matter interaction taking place in the proposed structures. Using this formalism we have systematically studied two realistic configurations based on an optically pumped Rb–ethane gas mixture and two types of numerically optimized nanophotonic systems, that is, a dielectric ring resonator and a plasmonic lattice. In both cases, we have shown how by tuning a photonic resonance to a suitable transition of the atomic cloud, it is possible to achieve coherent radiation at low power levels. In addition, using a simplified model, we have provided general guidelines for the design of hybrid nanophotonic lasers.

To the best of our knowledge, this is the first study of lasing action in such hybrid systems. Atomic–photonic hybrid systems are a rather novel and unexplored platform, and we believe the present study could stimulate further research aimed at exploiting their unique quantum optical properties. For instance, the study of the response of these hybrid systems in different light–matter coupling regimes, including strong coupling, is a promising future research direction that paves the way for realizing novel quantum optical phenomena and devices.

Supporting Information

Acknowledgements

Conflict of Interest

The authors declare no conflict of interest.

Keywords

[1] C. Santori, D. Fattal, J. Vuckovic, G. S. Solomon, Y. Yamamoto, *Nature* **2002**, *419*, 594.

[2] P. Michle, A. Kiraz, C. Becher, W. V. Schoenfeld, P. M. Petroff, L. Zhang, E. Hu, A. Imamoglu, *Science* **2000**, *290*, 2282.

[3] E. Moreau, I. Robert, J. M. Gerard, I. Abram, L. Manin, V. Thierry-Mieg, *Appl. Phys. Lett.* **2001**, *79*, 2865.

[4] G. S. Solomon, M. Pelton, Y. Yamamoto, *Phys. Rev. Lett.* **2001**, *86*, 3903.

[5] C. Santori, M. Pelton, G. Solomon, Y. Dale, Y. Yamamoto, *Phys. Rev. Lett.* **2001**, *86*, 1502.

[6] S. Noda, M. Yokoyama, M. Imada, A. Chutinan, M. Mochizuki, *Science* **2001**, *293*, 1123.

[7] X. Wu, A. Yamilov, X. Liu, S. Li, V. P. Dravid, R. P. H. Chang, H. Cao, *Appl. Phys. Lett.* **2004**, *85*, 3657.

[8] H. Altug, J. Vuckovic, *Opt. Express* **2005**, *13*, 8819.

[9] D. J. Bergman, M. I. Stockman, *Phys. Rev. Lett.* **2003**, *90*, 027402.

[10] M. Noginov, G. Zhu, A. M. Belgrave, R. Bakker, V. M. Shalaev, E. E. Narimanov, S. Stout, E. Herz, T. Suteewong, U. Wiesner, *Nature* **2009**, *460*, 1110.

[11] P. Berini, I. De Leon, *Nat. Photonics* **2012**, *6*, 16.

[12] O. Hess, J. B. Pendry, S. A. Maier, R. F. Oulton, J. M. Hamm, K. L. Tsakmakidis, *Nat. Mater.* **2012**, *11*, 573.

[13] R. M. Ma, R. F. Oulton, V. J. Sorger, X. Zhang, *Laser Photonics Rev.* **2013**, *7*, 1.

[14] S. M. Spillane, T. J. Kippenberg, K. J. Vahala, K. W. Goh, E. Wilcut, H. J. Kimble, *Phys. Rev. A* **2005**, *71*, 013817.

[15] T. Yoshie, A. Scherer, J. Hendrickson, G. Khitrova, H. M. Gibbs, G. Rupper, C. Ell, O. B. Shchekin, D. G. Deppe, *Nature* **2004**, *432*, 200.

[16] K. Hennessy, A. Badolato, M. Winger, D. Gerace, M. Atature, S. Gulde, S. Falt, E. L. Hu, A. Imamoglu, *Nature* **2007**, *445*, 896.

[17] M. Bajcsy, A. Majumdar, A. Rundquist, J. Vuckovic, *New J. Phys.* **2013**, *15*, 025014.

[18] K. Muller, A. Rundquist, K. A. Fischer, T. Sarmiento, K. G. Lagoudakis, Y. A. Kelaita, C. S. Munoz, E. del Valle, F. P. Laussy, J. Vuckovic, *Phys. Rev. Lett.* **2015**, *114*, 233601.

[19] A. Majumdar, D. Gerace, *Phys. Rev. B* **2013**, *87*, 235319.

[20] P. Lodahl, S. Mahmoodian, S. Stobbe, A. Rauschenbeutel, P. Schneeweiss, J. Volz, H. Pichler, P. Zoller, *Nature* **2016**, *541*, 473.

[21] A. Reiserer, G. Rempe, *Rev. Mod. Phys.* **2015**, *87*, 1379.

[22] B. Lang, R. Oulton, D. M. Beggs, *J. Opt.* **2017**, *19*, 045001.

[23] S. Mahmoodian, K. Prindal-Nielsen, I. Sãullner, S. Stobbe, P. Lodahl, *Opt. Mater. Express* **2017**, *7*, 43.

[24] N. Kalb, A. A. Reiserer, P. C. Humphreys, J. J. W. Bakermans, S. J. Kamerling, N. H. Nickerson, S. C. Benjamin, D. J. Twitchen, M. Markham, R. Hanson, *Science* **2017**, *356*, 928.

[25] F. Schmidt-Kaler, H. Haffner, M. Riebe, S. Gulde, G. P. T. Lancaster, T. Deuschle, C. Becher, C. F. Roos, J. Eschner, R. Blatt, *Nature* **2003**, *422*, 408.

[26] D. Leibfried, B. DeMarco, V. Meyer, D. Lucas, M. Barrett, J. Britton, W. M. Itano, B. Jelenkovic, C. Langer, T. Rosenband, D. J. Wineland, *Nature* **2003**, *423*, 412.

[27] J. Benhelm, G. Kirchmair, C. F. Roos, R. Blatt, *Nat. Phys.* **2008**, *4*, 463.

[28] P. W. H. Pinkse, T. Fischer, P. Maunz, G. Rempe, *Nature* **2000**, *404*, 365.

[29] A. Kuzmich, W. P. Bowen, A. D. Boozer, A. Boca, C. W. Chou, L. M. Duan, H. J. Kimble, *Nature* **2003**, *423*, 731.

[30] M. Wallquist, K. Hammerer, P. Rabl, M. Lukin, P. Zoller, *Phys. Scr.* **2009**, *T 137*, 014001.

[31] S. Du, M. B. Squires, Y. Imai, L. Czaia, R. A. Saravanan, V. Bright, J. Reichel, T. W. Hansch, D. Z. Anderson, *Phys. Rev. A* **2004**, *70*, 053606.

[32] T. Aoki, B. Dayan, E. Wilcut, W. P. Bowen, A. S. Parkins, T. J. Kippenberg, K. J. Vahala, H. J. Kimble, *Nature* **2006**, *443*, 671.

[33] T. G. Tiecke, J. D. Thompson, N. P. de Leon, L. R. Liu, V. Vuletic, M. D. Lukin, *Nature* **2014**, *508*, 241.

[34] W. Yang, D. B. Conkey, B. Wu, D. Yin, A. R. Hawkins, H. Schmidt, *Nat. Photonics* **2007**, *1*, 331.

[35] G. Epple, K. S. Kleinbach, T. G. Euser, N. Y. Joly, T. Pfau, P. S. J. Russell, R. Low, *Nat. Commun.* **2014**, *5*, 4132.

[36] A. D. Slepkov, A. R. Bhagwat, V. Venkataraman, P. Londero, A. L. Gaeta, *Phys. Rev. A* **2010**, *81*, 053825.

[37] R. Ritter, N. Gruhler, W. Pernice, H. Kubler, T. Pfau, R. Loew, *Appl. Phys. Lett.* **2015**, *107*, 041101.

[38] L. Stern, B. Desiatov, I. Goykhman, U. Levy, *Nat. Commun.* **2013**, *4*, 1548.

[39] S. A. Aljunid, E. A. Chan, G. Adamo, M. Ducloy, D. Wilkowsk, N. I. Zheludev, *Nano Lett.* **2016**, *16*, 3137.

[40] Z. Konefal, *Opt. Commun.* **1999**, 164.

[41] W. F. Krupke, R. J. Beach, V. K. Kanz, S. A. P. Lawrence, *Opt. Lett.* **2003**, *28*, 2336.

[42] W. F. Krupke, *Prog. Quantum Electron.* **2012**, *36*, 4.

[43] L. He, S. K. Ozdemir, L. Yang, *Laser Photonics Rev.* **2013**, *7*, 60.

[44] S. Maier, *Plasmonics: Fundamentals and Applications*, Word Scientific, Springer, New York, USA **2007**.

[45] A. E. Siegman, *Lasers*, University Science Books, Mill Valley, CA, USA **1986**.

[46] M. Sargent, M. O. Scully, W. E. Lamb, *Laser Physics*, Addison-Wesley, Reading, MA, USA **1974**.

[47] H. E. Tureci, A. D. Stone, B. Collier, *Phys. Rev. A* **2006**, *74*, 043822.

[48] M. Sukharev, A. Nitzan, *Phys. Rev. A* **2011**, *84*, 043802.

[49] S. L. Chua, Y. Chong, A. D. Stone, M. Soljacic, J. Bravo-Abad, *Opt. Express* **2011**, *19*, 1539.

[50] K. E. Dorfman, P. K. Jha, D. V. Voronine, P. Genevet, F. Capasso, M. O. Scully, *Phys. Rev. Lett.* **2013**, *111*, 043601.

[51] To solve the equations numerically, one has to seed the $a^+(0)$ at a very small value. This insures that the system of equations will evolve in

time and would not remain at the initial conditions given in Equation 11. The final results are checked to be completely independent from this seeding value.

[52] P. B. Johnson, R. W. Christy, *Phys. Rev. B* **1972**, *6*, 4370.

[53] W. Zhou, M. Dridi, J. Y. Suh, C. H. Kim, D. T. Co, M. R. Wasielewski, G. C. Schatz, T. W. Odom, *Nat. Nanotechnol.* **2013**, *8*, 506.

[54] F. van Beijnum, P. J. van Veldhoven, E. J. Geluk, M. J. A. de Dood, G. W. 't Hooft, M. P. van Exter, *Phys. Rev. Lett.* **2013**, *110*, 206802.

[55] J. Cuerda, F. Ruting, F. J. Garcia-Vidal, J. Bravo-Abad, *Phys. Rev. B* **2015**, *91*, 041118.

[56] T. K. Hakala, H. T. Rekola, A. I. Vakevainen, J. P. Martikainen, M. Necada, A. J. Moilanen, P. Torma, *Nat. Commun.* **2017**, *8*, 13687.

[57] J. Yablon, Z. Zhou, M. Zhou, Y. Wang, S. Tseng, M. S. Shahriar, *Opt. Express* **2016**, *24*, 27446.

[58] D. A. Steck, *Technical Report*, Los Alamos National Laboratory, Los Alamos, NM, USA **2001**.